Meshless helmholtz-hodge decomposition

Fabiano Petronetto[1,2],   Afonso Paiva[1,3,4],   Marcos Lage[1],
Geovan Tavares[1],   Hélio Lopes[1]   and   Thomas Lewiner[1]

[1] Department of Matematics — Pontifícia Universidade Católica — Rio de Janeiro — Brazil
[2] Department of Mathematics — Universidade Federal do Espírito Santo — Vitória — Brazil
[3] ICMC — USP — São Carlos — Brazil
[4] Faculty of Mathematics — Universidade Federal de Uberlândia — Brazil
www.matmidia.mat.puc--rio.br/~{fbipetro,apneto,mlage,tavares,lopes,tomlew}.

Abstract. Vector fields analysis traditionally distinguishes conservative (curl-free) from mass preserving (divergence-free) components. The Helmholtz-Hodge decomposition allows separating any vector field into the sum of three uniquely defined components: curl-free, divergence-free and harmonic. This decomposition is usually achieved by using mesh-based methods such as finite differences or finite elements. This work presents a new meshless approach to the Helmholtz-Hodge decomposition for the analysis of 2D discrete vector fields. It embeds into the SPH particle-based framework. The proposed method is efficient and can be applied to extract features from a 2D discrete vector field and to multiphase fluid flow simulation to ensure incompressibility.

Keywords: *Helmholtz-Hodge decomposition. Smoothed Particles Hydrodynamics. Vector fields. Features visualization. Multiphase fluids. Incompressible flow.*
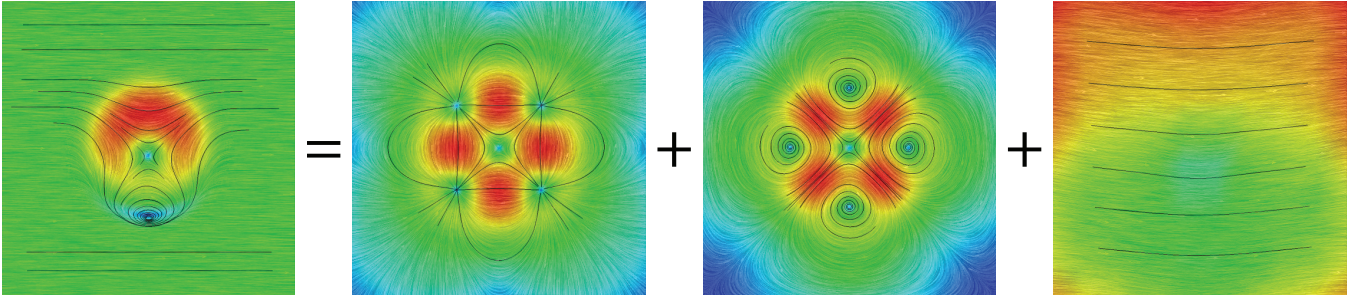
Figure 1: *Helmholtz-Hodge vector field decomposition using* SPH-HH *method, using LIC visualization with selected streamlines. From left to right: a vector field and its curl-free, divergence-free and harmonic components.*

1 Introduction

Vector fields are omnipresent in physics. They are often used to represent the velocity and direction of an object or the magnitude and direction of some force. Field features such as *sources*, *sinks* and *vortices* allow concise representation of the underlying flow phenomena. They can be identified by vector field decompositions such as *Helmholtz-Hodge decomposition*, which split a 2D discrete vector field into its curl-free and divergence-free component fields (Figure 1). The solution of this decomposition is given in terms of scalar potentials of a Poisson equation associated with each component field.

This simple process of the Helmholtz-Hodge decomposition provides many advantages in several Computer Graphics applications, such as the detection of vortices in flow images of the aerodynamic design of cars and aircrafts [20], estimation of motion fields on satellite images of tornadoes [6] and fluid flow simulation [19]. Traditionally, numerical solutions of Helmholtz-Hodge decomposition are provided by mesh-based methods, among them finite differences and finite elements. However, these methods are not suited to deal with sampling of point-vectors without an explicit connectivity between them or particle-based physical simulations. In this case, mesh-based methods would require the delicate task of topological map generation.

Related work

Polthier and Preuss [15] developed a discrete version of the 2D Helmholtz-Hodge decomposition. They used a global variational approach to compute independently two scalar valued potentials that determine the curl-free and divergence-free components of vector fields defined over surfaces. The main goal of their work is to detect singularities of vector fields by studying the critical points of the obtained potentials. They also presented a numerical algorithm based on the finite element method in [16] to implement the 2D field decomposition.

Tong *et al.* [20] extended the work of Polthier and Preuss for the decomposition of 3D fields on tetrahedral meshes. They also proposed a multiscale decomposition scheme that tries to improve the vector fields analysis by using different space-scales.

Although the algorithms proposed by these two works yield good performances, these implementations have high computational complexity as these techniques use irregular triangular or tetrahedral meshes, although they can reuse the Cholesky decomposition when decomposing several fields on the same mesh. In order to reduce the computational cost, Guo *et al.* [10] presented an efficient implementation for the discrete Helmholtz-Hodge decomposition, based on regular grids.

In the context of particle-based methods, Cummins and Rudman [22] introduced an SPH formulation of the Pressure Projection method to enforce incompressibility in fluid flow simulation based on the Helmholtz-Hodge decomposition. Later, Colin *et al.* [5] provided a new approximation of the pressure Poisson equation. In both works, the curl-free and harmonic components are neglected and only the irrotational component of a vector field is computed.

Contributions This work introduces a new meshless method to compute full Helmholtz-Hodge decomposition of 2D discrete vector fields on arbitrary unstructured sets of point-vectors. Our method uses the particle-based framework of *Smoothed Particle Hydrodynamics* (SPH) to obtain a smooth approximation of the differential operators utilized in Helmholtz-Hodge decomposition. We show the efficiency and versatility of the proposed method in typical applications, such as visualization and analysis of a 2D velocity field to incompressible multiphase fluid flow simulation. To the author's knowledge, this work is the first proposal for vector field decomposition directly from particles.

Outline We provide a mathematical background of the Helmholtz-Hodge decomposition in the next section. In section 3, we give a brief introduction of the SPH method. section 4 introduces an SPH approximation of the Poisson equation. Later, we show the details of the implementation of the proposed method in section 5. Results from different applications of the new method are given in section 6. Finally, section 7 concludes this paper with a brief discussion about the proposed method and a glimpse on future works.
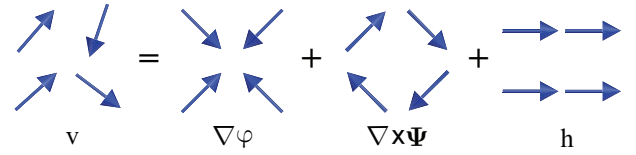
2 Helmholtz-Hodge Decomposition

Figure 2: *The Helmholtz-Hodge decomposition of a 2D discrete vector field* **v**.

The Helmholtz-Hodge decomposition theorem [4] from vectorial analysis states that any vector field **v** can be decomposed *uniquely* into three component vector fields:

$$\mathbf{v} = \mathbf{d} + \mathbf{r} + \mathbf{h}, \tag{1}$$

where the component **d** is curl-free, **r** is divergence-free and **h** is harmonic , whose curl and divergence both vanish:

$$
\begin{aligned}
\nabla \times \mathbf{d} &= 0 \\
\nabla \cdot \mathbf{r} &= 0 \\
\Delta \mathbf{h} &= 0
\end{aligned}
$$

The decomposition is actually built from a scalar potential φ and a vector potential $\boldsymbol{\Psi}$: $\mathbf{d} = \nabla\varphi$ and $\mathbf{r} = \nabla \times \boldsymbol{\Psi}$, with $\mathbf{h} = \mathbf{v} - \mathbf{d} - \mathbf{r}$. This decomposition is illustrated in Figure 2.

In the bidimensional case, the decomposition of vector fields requires a particular definition introduced by Polthier and Preuss [16]. Let J be an operator on vector fields which rotates every vector by $90°$ in clockwise order

$$J(\mathbf{v}) = J(v_1, v_2) = (v_2, -v_1). \tag{2}$$

The Helmholtz-Hodge decomposition for a 2D vector field is given by

$$\mathbf{v} = \nabla\varphi + J(\nabla\psi) + \mathbf{h}. \tag{3}$$

Actually in 2D, a divergence-free field is obtained by computing the gradient of a scalar potential ψ and then applying the J operator[16].

In the bidimensional space, the curl operator is defined by

$$\nabla \times \mathbf{v} = \nabla \times (v_1, v_2) = \frac{\partial v_2}{\partial x} - \frac{\partial v_1}{\partial y}$$

and by using Eq.(2), we can rewrite it as

$$\nabla \times \mathbf{v} = (\nabla \cdot J)\mathbf{v}. \tag{4}$$

Moreover, we have the following properties in the bidimensional case:

1. The component $\mathbf{d} = \nabla\varphi$ is a curl-free vector field

$$(\nabla \cdot J)\mathbf{d} = 0.$$

2. The component $\mathbf{r} = J(\nabla\psi)$ is a divergence-free vector field

$$\nabla \cdot \mathbf{r} = 0.$$

3. The component $\mathbf{h}$ is a harmonic field

$$\nabla \cdot \mathbf{h} = (\nabla \cdot J)\mathbf{h} = 0.$$

These properties lead to the following Poisson equation system

$$\begin{cases} \nabla \cdot \mathbf{v} &= \Delta\varphi \\ (\nabla \cdot J)\mathbf{v} &= -\Delta\psi \end{cases}, \qquad (5)$$

where the potentials φ and ψ of Eq.(3) are solutions of the system.

For closed domains, the unicity of the potentials φ and ψ is guaranteed by adding to the Poisson equation system above a boundary condition. The usual condition forces the curl-free component to be tangent to the boundary, and the divergence-free component perpendicular to it:

$$\frac{\partial\varphi}{\partial\mathbf{n}} = 0, \qquad \frac{\partial\psi}{\partial\mathbf{n}} = 0, \qquad (6)$$

where $\mathbf{n}$ is the normal at the boundary (observe that $\frac{\partial\varphi}{\partial\mathbf{n}} = \nabla\varphi \cdot \mathbf{n}$). We used this condition for all the results of this paper, except in Figure 1. Another possible boundary condition, used in Figure 1, is to impose constant potentials on the boundary, which means a curl-free component perpendicular to the boundary and the divergence-free tangent to it.
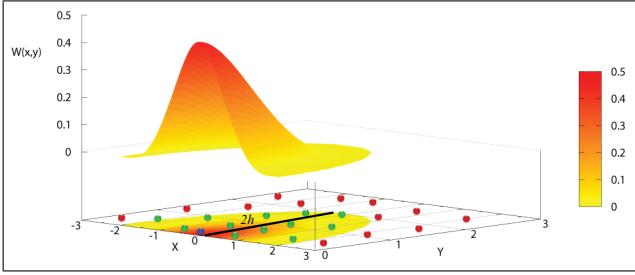
3 Smoothed Particles Hydrodynamics

Figure 3: *Quartic smoothing kernel: the particles farther than the smoothing length $2h$ are discarded.*

The main idea of SPH approximation is to represent a physical system as a set of particles that occupy spatial positions and carry individual physical *attributes*, such as velocity, pressure, mass, density. The attributes at point $\mathbf{x}$ are computed by using a kernel function with compact support as follows:

$$\langle\, f\,\rangle_h (\mathbf{x}) = \sum_{j \in N(\mathbf{x})} \frac{m_j}{\rho_j} f(\mathbf{x}_j) W(\mathbf{x} - \mathbf{x}_j, h) \qquad (7)$$

where set $N(\mathbf{x})$ contains all the particles at a distance below a multiple of h from $\mathbf{x}$, j is the particle index, $\mathbf{x}_j$ the particle position, m_j the particle mass and ρ_j the particle density.

For the illustrations and experiments of this work, we choose a piecewise quartic smoothing kernel function (see Figure 3) with a smoothing length of twice the initial particle spacing h.

$$W(\mathbf{x} - \mathbf{x}_j, h) = \frac{15}{7\,\pi\,h^2} \cdot w\left(\frac{\|\mathbf{x} - \mathbf{x}_j\|}{h}\right) \qquad \text{with}$$

$$w(q) = \begin{cases} \frac{2}{3} - \frac{9}{8}q^2 + \frac{19}{24}q^3 - \frac{5}{32}q^4 & ; \quad 0 \le q \le 2 \\ 0 & ; \qquad q > 2 \end{cases}$$

The reader can find a complete discussion about kernel functions in [25, 27] and a wide overview of SPH method in Monaghan's survey [26].

The SPH method approximates the differential operators appearing in partial differential equations of the physical system through discrete convolutions with the kernel derivatives. In this work, we choose the following formulations of the operators

Gradient

$$\nabla f_i = \sum_{j \in N_i} \frac{m_j}{\rho_j} (f_j - f_i) \nabla_i W(\mathbf{x}_i - \mathbf{x}_j, h) \qquad (8)$$

Divergence

$$\nabla \cdot \mathbf{f}_i = \sum_{j \in N_i} \frac{m_j}{\rho_j} (\mathbf{f}_j - \mathbf{f}_i) \cdot \nabla_i W(\mathbf{x}_i - \mathbf{x}_j, h) \qquad (9)$$

Laplacian

$$\Delta f_i = \sum_{j \in N_i} 2\frac{m_j}{\rho_j} \frac{(f_i - f_j)}{\|\mathbf{x}_{ij}\|^2} \mathbf{x}_{ij} \cdot \nabla_i W(\mathbf{x}_i - \mathbf{x}_j, h) \qquad (10)$$

where $\mathbf{x}_{ij} = \mathbf{x}_i - \mathbf{x}_j$.

This choice is motivated by the mathematical relevance and computational efficiency of those operators. In the first author's thesis [14], the most common operators of the SPH literature [24] are compared with their analytical smooth counterparts both in terms of differential qualities and numerical accuracy. The SPH operators listed above shown the best results in various experiments, varying the input field and the density and distribution of the particles. In particular in 2D, the most accurate Laplacian approximations are the above one (Eq.(10)) and the composition of the SPH operators $\nabla\cdot$ and ∇ [14]. We chose the first one since it is less computationally intensive, requiring only one neighborhood for each particle.

4 SPH Poisson Equation

In this section, we introduce the SPH approximation to solve Poisson's equation:

$$\Delta\phi(\mathbf{r}) = f(\mathbf{r}) \qquad (11)$$

where f and ϕ are real functions over a domain $\Omega \subset \mathbb{R}^2$.

The *SPH Poisson equation* is constructed by taking a point-set $S = \{\mathbf{x}_1, \mathbf{x}_2, \cdots, \mathbf{x}_n\} \subset \Omega$ and by replacing the Laplacian operator in Eq.(11) by SPH Laplacian operator (Eq.(10)). Thus, given a point $\mathbf{x}_i \in S$, the SPH Poisson equation is denoted by

$$\sum_{j \in N_i} 2\frac{m_j}{\rho_j} \frac{(\phi_i - \phi_j)}{\|\mathbf{x}_{ij}\|^2} \mathbf{x}_{ij} \nabla_i W_{ij} = f(\mathbf{x}_i). \qquad (12)$$

Using the kernel properties, Eq.(12) can be written as

$$\sum_{j \in N_i} 2\frac{m_j}{\rho_j} (\phi_i - \phi_j) F(\mathbf{x}_{ij}) = f(\mathbf{x}_i) \qquad (13)$$

$$\text{with} \quad F(\mathbf{x}_{ij}) = \frac{15}{7\,\pi\,h^2} \frac{1}{h\,\|\mathbf{x}_{ij}\|} \frac{\partial w}{\partial r}(\mathbf{x}_{ij}) \quad r = \frac{\|\mathbf{x}_{ij}\|}{h}.$$
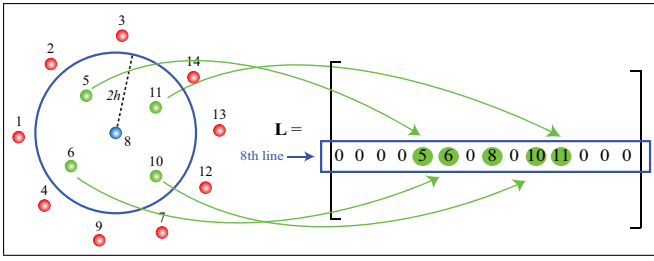
Figure 4: *Building the sparse matrix $\mathbf{L}$: the 8th line of $\mathbf{L}$ has null coefficients in the columns where the points are in a greater distance than $2h$ from the point $\mathbf{x}_8$.*

Observe that F is measured as a distance to the power -5, and multiplied by the volume in the expression of f it has the dimension m^{-2}, which is coherent for representing the second-order space derivatives of the Laplacian.

Eq.(13) for all points of S determine the unknown potentials values $\boldsymbol{\phi}$, leading to the linear system $\mathbf{L}\boldsymbol{\phi} = \mathbf{b}$. The i-th line of the matrix $\mathbf{L}$ is obtained through Eq.(13) at point $\mathbf{x}_i \in S$ with coefficients

$$
\begin{cases}
a_{ij} = -2\dfrac{m_j}{\rho_j} F(\mathbf{x}_{ij}) \quad, \quad j \neq i \\
a_{ii} = -\displaystyle\sum_{k \neq i} a_{ik}
\end{cases}
$$

and the coefficients of the vector $\mathbf{b}$ are given by $f(\mathbf{x}_i)$.

Note that, at line i of $\mathbf{L}$, the coefficient a_{ij} at j-th column is not null if, and only if, the distance between the points $\mathbf{x}_i$ and $\mathbf{x}_j$ is less than the smoothing length $2h$, leading to a very sparse matrix (see Figure 4).

The boundary condition, such as Eq.(6), are directly incorporated into the system for particles i closer than $\frac{1}{\pi}\sqrt{\frac{m_i}{\rho_i}}$ from the boundary. Instead of replacing Eq.(13) by the boundary condition $\nabla\phi \cdot \mathbf{n} = 0$, which would consider the particle to lay *exactly* on the boundary, we add up to the right-hand side of Eq.(13) the term $\nabla\phi \cdot \mathbf{n}$, which leads to a smoother transition. Furthermore, the normal $\mathbf{n}$ is computed averaging the neighboring boundary normals.

5 Decomposition Algorithm

In section 2, we saw that a vector field $\mathbf{v}$ can be decomposed as $\mathbf{v} = \mathbf{d} + \mathbf{r} + \mathbf{h}$, where the components $\mathbf{d}$ and $\mathbf{r}$ are obtained by computing the scalar potentials φ and ψ defined by System (5). Each equation in this system can be solved independently through a linear system (see section 4). Now we are going to enumerate the main steps of the Helmholtz-Hodge decomposition by using the SPH method (Figs. 6 and 7). We call this method SPH-HH.

(a) Setup vector field

Let $\mathcal{V} = \{\mathbf{v}_1, \mathbf{v}_2, \cdots, \mathbf{v}_n\}$ be a discrete vector field defined in $\Omega \subset \mathbb{R}^2$, where $\mathbf{v}_i = \mathbf{v}(\mathbf{x}_i)$ with $\mathbf{x}_i \in \Omega$. Each vector $\mathbf{v}_i$ is associated with an SPH particle indexed by i and positioned at $\mathbf{x}_i$. The mass attribute is defined constant in all particles given by mass $m = V_\Omega/n$ with $V_\Omega = Volume(\Omega)$.

Finally, the density in each particle i is computed directly from Eq.(7):

$$
\rho_i = \sum_{j \in N(\mathbf{x}_i)} m_j W(\mathbf{x}_i - \mathbf{x}_j, h) .
$$

The left column of Figure 6 shows a synthetic vector field represented by 493 vectors.
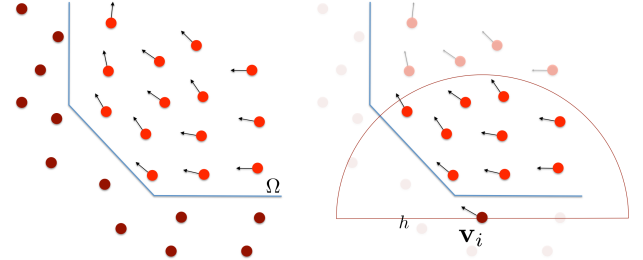

Figure 5: *The fake particles (left) in the SPH-HH method avoid inaccuracy in the SPH approximations (right).*

(b) Boundary deficiency compensation

The SPH operators at particles close to the boundary may suffer from the lack of particles in specific directions. To go around this problem, we create fake particles (Figure 5) off the boundary using a Poisson disk sampling [8]. The original vector field $\mathbf{v}$ is extended to those fake particles by a Chen-Beraun corrected SPH approximation [24]:

$$
\mathbf{v}_i^{fake} = \frac{\displaystyle\sum_{j \in N(\mathbf{x}_i)} \frac{m_j}{\rho_j} \mathbf{v}_j W(\mathbf{x}_i - \mathbf{x}_j, h)}{\displaystyle\sum_{j \in N(\mathbf{x}_i)} \frac{m_j}{\rho_j} W(\mathbf{x}_i - \mathbf{x}_j, h)} , \qquad (14)
$$

where the summation is taken over the original particles samples neighbors of a fake particle.

Figure 5 shows an example of the fake particles generation and illustrate the extension of $\mathbf{v}$ in a fake particle.

To avoid including the fake particles as extra equations in the linear system, which would require computing derivatives at their locations, we substitute them by original potential unknowns using the same correction as follows. Given a particle i, when a neighboring particle j is a fake particle, then the potential ϕ_j, in the SPH Laplacian approximations (Eq.(13)) is replaced by

$$
\phi_j = \frac{\displaystyle\sum_{k \in N_j} \frac{m_k}{\rho_k} \phi_k W_{jk}}{\displaystyle\sum_{k \in N_j} \frac{m_k}{\rho_k} W_{jk}}
$$

where the summation is taken over the original particles.

Observe that this approximation may suffer if the boundary is thinner than h. As usually in SPH, the smoothing length h and the particle density must be adapted to avoid that case.
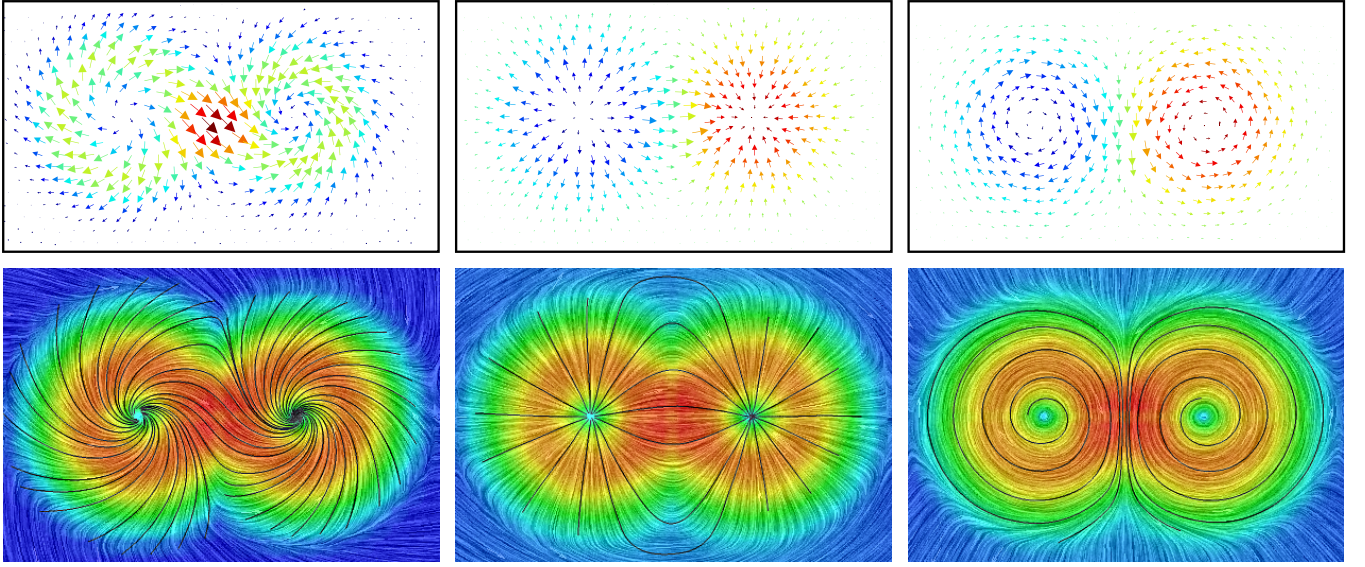
Figure 6: *Helmholtz-Hodge decomposition of a vector field* **v** *(left column) in a curl-free component* **d** *(middle column) and a divergence-free component* **r** *(right column). We can see the vector fields at some of the* 18221 *samples (top) and the magnitude map color with some streamlines (bottom).*

(c) Curl-free component

The curl-free component **d** is obtained by SPH gradient approximation of the potential φ given by the Poisson equation

$$\Delta\varphi = \nabla \cdot \mathbf{v}\,,$$

including the boundary condition discussed above.

Solving the SPH Poisson equation, including the boundary condition $\nabla\varphi\cdot\mathbf{n} = 0$, as described in section 4, we obtain the potential φ. Finally, the curl-free component is computed from Eq.(8) by:

$$\mathbf{d}_i = \nabla\varphi_i = \sum_{j \in N_i} \frac{m_j}{\rho_j} \left(\varphi_j - \varphi_i\right) \nabla_i W_{ij}\,. \qquad (15)$$

The middle column of Figure 6 shows a curl-free component of a synthetic field represented by 493 vectors.

(d) Divergence-free component

The divergence-free component is obtained in the same way as of the curl-free component. We first solve the Poisson equation associated with potential ψ

$$\Delta\psi = -(\nabla \cdot J)\mathbf{v}\,,$$

including the boundary condition $\frac{\partial\psi}{\partial\mathbf{n}} = 0$. Then, we use the SPH gradient operator (Eq.(8))

$$\nabla\psi_i = \frac{1}{\rho_i} \sum_{j \in N_i} m_j \left(\psi_j - \psi_i\right) \nabla_i W_{ij}\,,$$

to compute the divergence-free component $\mathbf{r}_i = J(\nabla\psi_i)$, by applying the J operator (Eq.(4)) to $\nabla\psi_i$.

The right column of Figure 6 shows a divergence-free component of a syntheti field represented by 493 vectors.

(e) Harmonic component

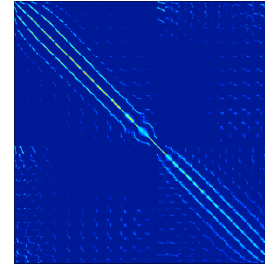After computing the divergence-free and curl-free components, the harmonic component is determined by

$$\mathbf{h} = \mathbf{v} - \mathbf{d} - \mathbf{r}\,.$$

For example, the synthetic field illustrated in Figure 7(a) is built analytically as the sum of three components: divergence-free, curl-free and a large, almost constant harmonic fields. Figure 7(b) shows the sum of the divergence-free and the curl-free components obtained by our SPH-HH method, and Figure 7(c) shows the harmonic part, which has been consistently identified.

6 Results and Applications

Most of the vector fields shown along this paper are given by non-uniform samples, except in Figs. 7 and 16. To better visualize them, we either display a sparser sampling of the field (Figs. 6, 7, 13, 15, 16 and 17), or use an artistic illustration of the fields (LIC), where colors represent the vector magnitudes (Figs. 1, 6, 8 and 14). On some of the illustrations, we further show some manually selected streamlines, computed through a local vector field reconstruction [13].

(a) Decomposition results

We implemented the SPH-HH technique following the previous description. We use iterative solvers for the linear system since they present a double advantage. Firstly, due to the high degree of sparseness of matrix **L**, such solvers are well adapted. For example, the side figure shows the matrix structure

(a) Vector Field   (b) Free Components: $\mathbf{d} + \mathbf{r}$ (c) Harmonic Component
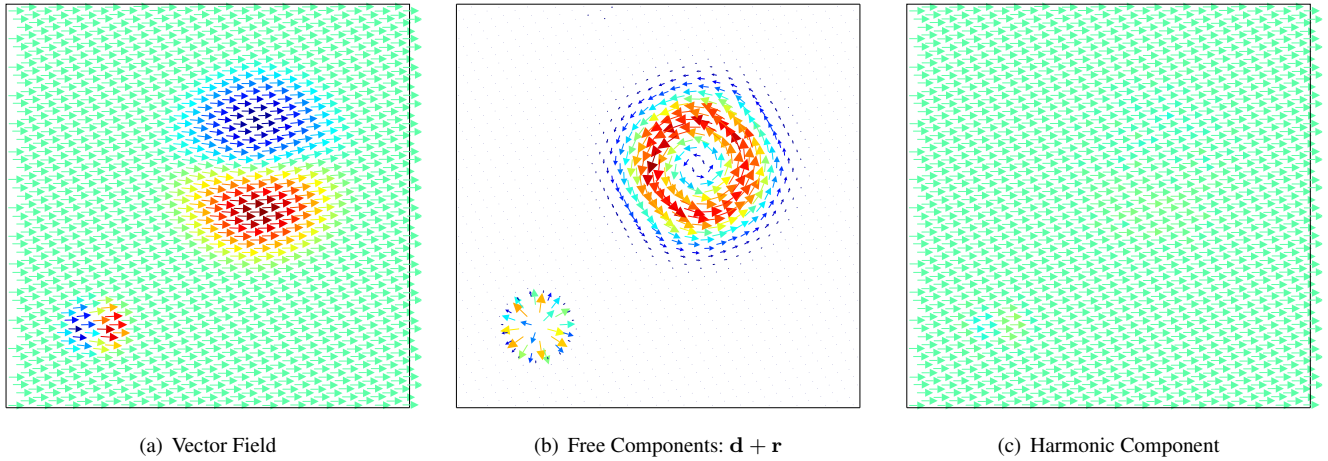
Figure 7: *The SPH-HH method reveals the divergence-free $\mathbf{r} = J(\nabla\psi)$ and the curl-free $\mathbf{d} = \nabla\varphi$ components before the decomposition of the 2D vector field (left) even with a large harmonic part, constant equal to $10\max(\|\mathbf{r}\|, \|\mathbf{d}\|)$ (hedgehog visualization using $\frac{1}{3}$ of the samples).*
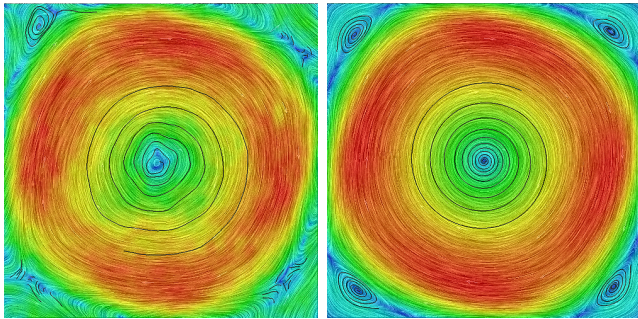

Figure 8: *The divergence-free component obtained by SPH-HH method with (right $\kappa = 0.001$) and without ridge regression (RR) technique (left, $\kappa = 0$). Some small scale vortices of a single frame of bidimensional incompressible flow are not seen in the corners of a vector field decomposition without RR technique. The RR improves the stability of the decomposition.*

Execution Time				
			iterations	
# Particles	κ	time (sec)	curl-free	div-free
1640	10^{-8}	4.31	1234	629
	10^{-2}	2.23	476	477
5000	10^{-8}	37.78	2609	636
	10^{-2}	9.53	407	411
18221	10^{-8}	130.39	683	582
	10^{-2}	78.95	393	391

Tab. 9: *The execution time to Helmholtz-Hodge decomposition given by SPH-HH method in the synthetic field of Tab. 6 with different density of particles. The target residual of the iterative method is set to 10^{-6}.*

on the field illustrated in Figure 8. Secondly, several iterative methods converge very fast if initialized close to the solution. In simulation contexts, a good initialization can be easily obtained from the previous time step.

More precisely, we use the `SparseLib++` package [17] to storage the matrix and the vectors. The linear system is solved by using an iterative method from the `IML++` package [7]. Moreover, the boundary conditions induce asymmetries in the matrix, and we thus use a quasi-minimal residual method [18] in our implementation.

Finally, matrix $\mathbf{L}$ (built in section 4) may be ill-conditioned, since it partly corresponds to a Laplacian operator (each line sums up to *zero*). We use a *ridge regression* (RR) technique to stabilize the system [12]. This technique adds to matrix $\mathbf{L}$ the scaled identity matrix $\kappa\mathbf{I}$. We thus solve the linear system $(\mathbf{L} + \kappa\mathbf{I})\tilde{\phi} = \mathbf{b}$, which, for small values of κ, induces very small perturbation of the result. In the exampled of this work, the order of magnitude of the coeffi-

cients of matrix $\mathbf{L}$ is a few hundreds, while κ is set to much smaller values, typically 10^{-3}. This leads to a fast, in-place Helmholtz-Hodge decomposition for particle systems.

Figure 8 shows the results obtained with and without RR technique for the vector field decomposition of a single frame of a bidimensional vortex spin-down simulation (11500 samples). Note that some small scale vortices are not seen in the corners without RR, while the use of the RR technique significantly improved the result. The execution times are reported on Table 9 for the single data of Figure 6.

(b) Analysis of the numerical results

In this section, we analyze numerically how the decompositions obtained by our SPH-HH method satisfy the properties stated in section 2.

In Figs. 10 and 11, we analyze the vector field of Figure 1, sampled with 10000 points. The right histogram shows of the divergence of component $\mathbf{r}$ ($\nabla \cdot \mathbf{r} = 0$) obtained by an SPH-HH decomposition. Similarly, the left histogram shows the curl of component $\mathbf{d}$ ($\nabla \times \mathbf{d} = 0$). Those differential
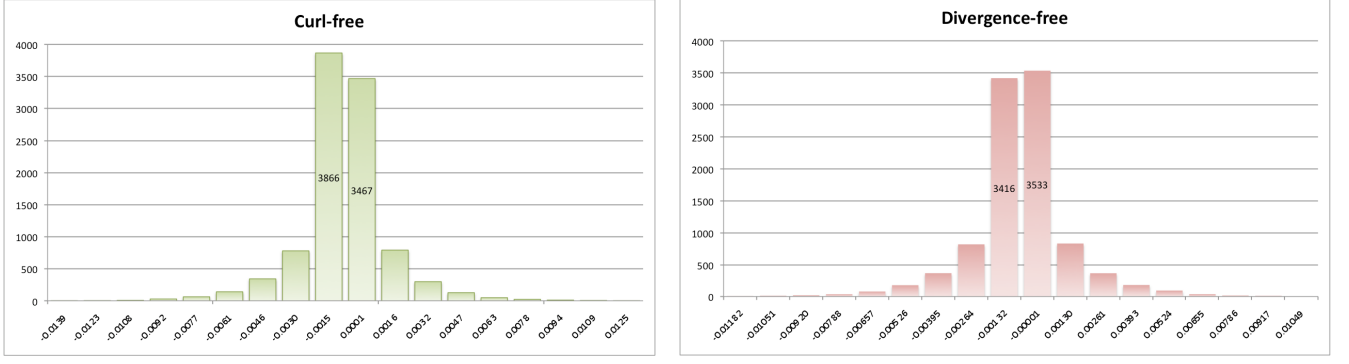
Figure 10: *The differential properties of the curl-free $\nabla \times \mathbf{d}$ (left) and divergence-free $\nabla \cdot \mathbf{r}$ (right) components given by our SPH-HH method in the vector field decomposition illustrated in Figure 1, represented as a histogram number of particles vs. the SPH differential approximation that should vanish on the component. Both distributions are concentrated at low values of this error.*
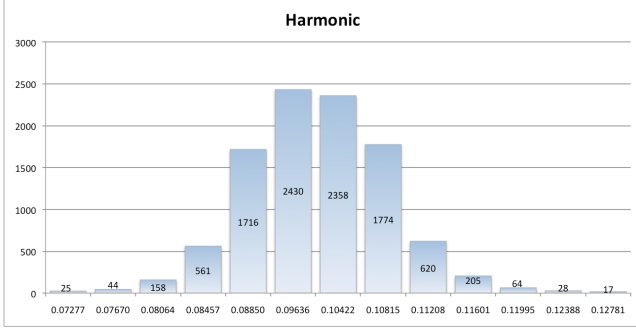

Figure 11: *The magnitude of the harmonic component obtained in the SPH-HH decomposition of the vector field with constant harmonic field ($\|\mathbf{h}\| = 0.1$).*

properties are given by the operators SPH (Eqs. (8) and (9)) and Eq.(2)). Both distributions are concentrated around zero, which is the expected value.
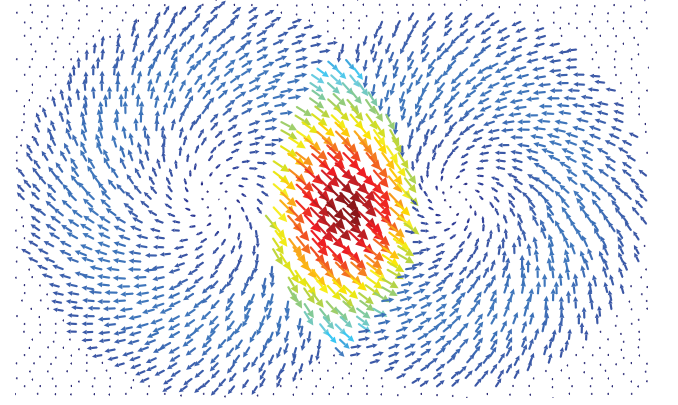
The original vector field $\mathbf{v}$ has a harmonic component of constant magnitude ($\|\mathbf{h}\| = 0.1$), and Figure 11 shows the magnitude of the harmonic component obtained by the SPH-HH decomposition. The harmonic magnitude is actually concentrated around 0.1.

We also compute the global $\mathcal{L}^2$-orthogonality between the curl-free and divergence-free components of the SPH-HH decomposition, as given by the SPH approximation

$$\int_\Omega <\mathbf{r}, \mathbf{d}> \mathrm{d}\Omega = \sum_j \frac{m_j}{\rho_j} <\mathbf{r}_j, \mathbf{d}_j> . \qquad (16)$$

For the vector field of Figure 1, the scalar product is $3.74.10^{-4}$ (for an average magnitude of 0.02) and $1.56.10^{-6}$ for the vector field of Figure 6 (average magnitude of 0.01), the components are numerically orthogonal.

We performed further numerical analysis of the error, as compared to the analytical solution (Figure 12). We can observe that the relative error as compared to the analytical decomposition is of the order of a few percents, while the residual of the linear solver was set to 10^{-6}. This shows that most of the approximation error does not come from the linear solver, but rather from the SPH approximations directly.

Error measures				
	max	mean	var	median
$\|d - d_0\|$	$2.88 \ 10^{-2}$	$6.27 \ 10^{-3}$	$1.99 \ 10^{-5}$	$5.18 \ 10^{-3}$
$\frac{\|d - d_0\|}{\|v0\|}$	$6.31 \ 10^{-1}$	$8.92 \ 10^{-2}$	$4.90 \ 10^{-3}$	$7.21 \ 10^{-2}$
$\|r - r_0\|$	$2.89 \ 10^{-2}$	$5.92 \ 10^{-3}$	$2.12 \ 10^{-5}$	$4.59 \ 10^{-3}$
$\frac{\|r - r_0\|}{\|v0\|}$	$4.38 \ 10^{-1}$	$8.06 \ 10^{-2}$	$4.22 \ 10^{-3}$	$6.34 \ 10^{-2}$
$\|h\|$	$3.85 \ 10^{-2}$	$8.88 \ 10^{-3}$	$3.84 \ 10^{-5}$	$7.35 \ 10^{-3}$
$\frac{r \cdot d}{\|r\| \ \|d\|}$	$5.05 \ 10^{-1}$	$3.50 \ 10^{-2}$	$1.38 \ 10^{-3}$	$2.73 \ 10^{-2}$
$\nabla \cdot d$	$1.00 \ 10^{-1}$	$3.83 \ 10^{-5}$	$3.28 \ 10^{-4}$	$3.29 \ 10^{-4}$
$\nabla \times r$	$1.00 \ 10^{-1}$	$3.66 \ 10^{-5}$	$3.29 \ 10^{-4}$	$2.17 \ 10^{-4}$
$\|v0\|$	$1.52 \ 10^{-1}$	$7.55 \ 10^{-2}$	$5.60 \ 10^{-4}$	$7.20 \ 10^{-2}$

Figure 12: *Numerical analysis of the error on an analytic vector field generated with 13287 particles, containing two sources and two vortices (top figure). The subindices 0 refer to the analytical solution. In this case, the error of Eq.(16) was $2.13 \ 10^{-6}$.*

(c) Feature-based visualization

The increasing amounts of vector fields generated by simulations lead to a delicate visualization problem, which is nicely described by Helman and Hesselink [11]. The data represented by standard techniques like hedgehogs (a small arrow for every vector in a given vector field) or streamlines (also known as integral curves) may not be very informative: a raw hedgehog with millions of arrows or 3D streamlines in 3D may be confused. There are two main possibilities to avoid this problem. The first one, proposed by Helman and Hesselink [11], is to emphasize the vector field topology [3, 21].
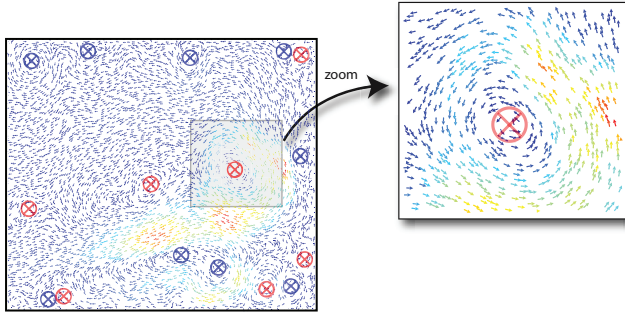

Figure 13: *Feature-based visualization. The SPH-HH method detects the vortex in a vector field (visualized on 8000 particles, $\frac{1}{4}$ of all the particles), focusing only on the areas or points, which are characteristics of the flow.*

Computing the locations of specific features of the flow and merely showing these features by using lines, points or other appropriate primitive graphical objects, is a second possibility. It is called *feature-based visualization*. Instead of millions of small arrows or thousands of knotted streamlines, one only visualizes the areas or points which are characteristics of the flow (Figure 13).

Furthermore, field features visualization provides easier insight into the data for engineers and scientists. For example, as the behavior of the flow around a moving body is responsible for the aerodynamic resistance, fluid dynamical experiments are important for car and plane design. For example, in the case of aircrafts, the vortices are fundamental for the lifting capacity (Figure 14). The Helmholtz-Hodge decomposition is particularly interesting to obtain the features in a vector field. In the bidimensional case solved in this work, both components are given by scalar potentials (Eq.(3)). The singularities of each potential, i.e., the points where a component is null, are obtained automatically in the SPH-HH method by tracking particle locations reaching a local minimum or maximum of the potentials φ or ψ.

The singularities in the curl-free component $\mathbf{d} = \nabla\varphi$ are centers of sinks (resp. sources) for maxima (resp. minima) of φ (Figure 15). For the divergence-free component $\mathbf{r} = J\left(\nabla\psi\right)$, the singularities are centers of clockwise (resp. counter-clockwise) vortices for minima (resp. maxima) of ψ.
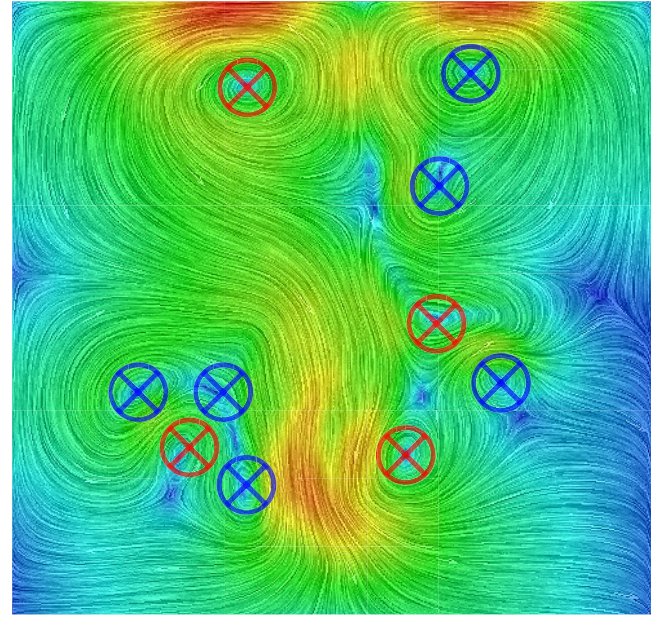

Figure 14: *The SPH-HH method detects the vortex cores in a velocity vector field sampled by 6400 particles from an incompressible fluid flow simulation.*

We further study the SPH-HH decomposition on non simply-connected regions. Figure 16 shows a frame of a simulation of fluid-rigid body interaction using fictitious domain (blank shape) with finite element method based on a distributed Lagrange multiplier [9]. The decomposition detects the vortices' centers even with the complex boundary of the rigid body.

Figure 17 shows the decomposition of a turbulent velocity field around a rigid object [2], where a rotating component around the hole is artificially included. (a) shows the normalized vector field with our automatic feature detection. The divergence-free component and the harmonic field are illustrated in (b) and (c). The non-trivial harmonic field extracted shows a very coherent, circular set of vectors that rotates around the hole, which is characteristic of such topologies.
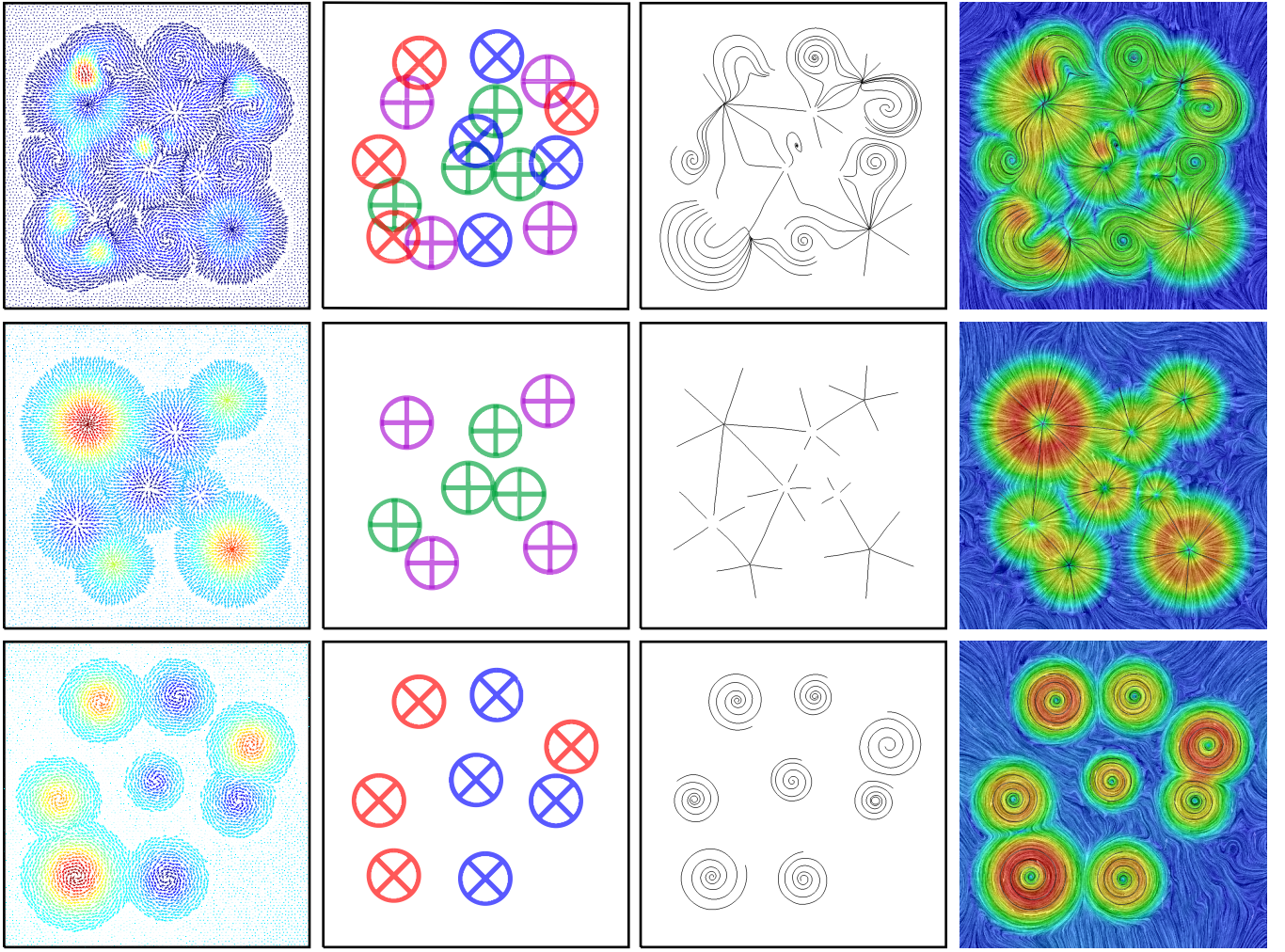
Figure 15: *The singularities of each component are obtained automatically from the* SPH-HH *method through the critical points of the potentials φ and ψ, visualized using all the 5001 particles. The features in the curl-free component $\mathbf{d} = \nabla\varphi$ (middle row) are centers of sinks at maxima of φ (purple marks) and centers of sources at minima of φ (green marks). For the divergence-free component $\mathbf{r} = J(\nabla\psi)$ (bottom row) are vortices centered at the critical points of ψ: clockwise for a minimum (blue marks) and counter-clockwise for a maximum (red marks).*

(d) Fluid flow simulation

Computing divergence-free velocity field is of great importance in this application due to its physical meaning of mass conservation. A fluid flow with this restriction is called *incompressible*.

Stam in his seminal work on *stable fluids* [19] introduced in Computer Graphics a *projection method* based on the Helmholtz-Hodge decomposition to simulate incompressible fluids by using a semi-Lagrangian scheme to discretize the convective term of Navier-Stokes equation. This method consists in projecting a velocity field without null divergence $\mathbf{v}^*$ into divergence-free space in each time step dt. This projection is given explicitly by the solution of a pressure Poisson equation with pure Neumann boundary condition:

$$\Delta p = \frac{1}{dt}\nabla \cdot \mathbf{v}^* \quad \text{with} \quad \frac{\partial p}{\partial \mathbf{n}}\big|_{\partial\Omega} = 0 \,,$$
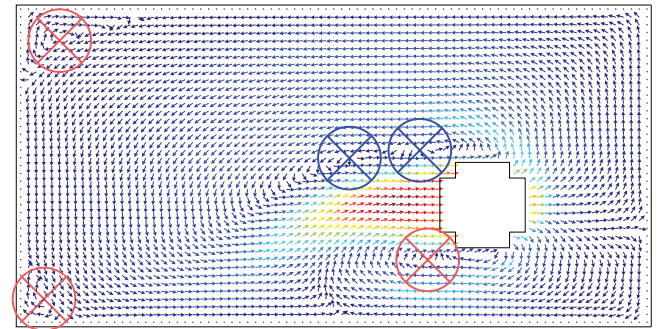

Figure 16: *The* SPH-HH *method with complex boundaries, sampled with 3216 particles. Incompressible velocity field of a simulation of fluid-rigid body interaction*

(a) Normalized Vector Field.   (b) Solenoidal Component.   (c) Harmonic Component.
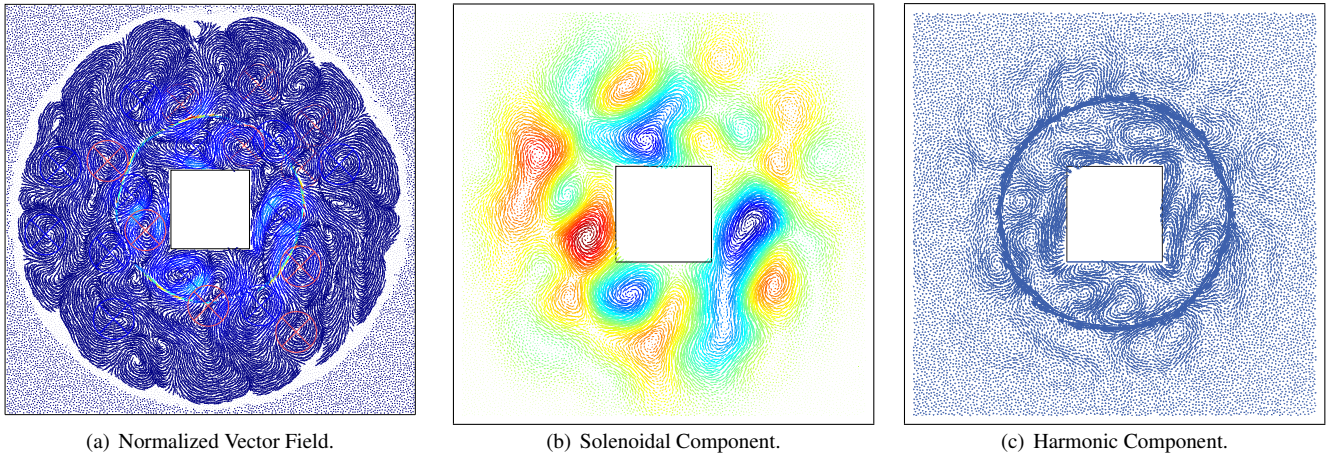
Figure 17: *The SPH-HH decomposition of a turbulent field around rigid object, sampled with 23267 particles, where an artificial rotation around the hole is added. The harmonic component correctly extracts this rotation, which is characteristic of such topologies.*

where p is the pressure of the fluid and $\mathbf{n}$ is the normal at boundary $\partial\Omega$ of the problem domain Ω.

Unlike previous methods, the SPH fluid animation frameworks [1, 23, 27, 28, 29] only solve compressible fluid flows, where the pressure is computed using a state equation in terms of density and speed of sound in the fluid. We can use the SPH-HH method to obtain a velocity field with divergence-free in a way similar to projection methods [5, 22, 19] in order to enforce incompressibility in traditional SPH fluid flow frameworks.

We can see in Figs. 18 and 19 the results of the two-phase immiscible fluid flow simulations using the SPH-HH method to update the pressure. The first simulation reveals the shape evolution of a *rising droplet* in a heavier fluid (see Figure 18). When a light fluid droplet is merged in the heavy fluid, due to the density difference, the pressure computed by SPH-HH method leads to the buoyancy force acting on the droplet that generates an upward motion and deforms it.

Finally, we simulate *Rayleigh-Taylor instability* (see Figure 19). This instability occurs when heavy fluid is being accelerated into a light fluid due to a gravitational field. Again, we update the pressure field by using the SPH-HH method and compute the velocity field with null divergence in each time step of the simulation.

7 Conclusion and Future Works

This work introduces a new meshless approach of the Helmholtz-Hodge decomposition of 2D discrete vector fields. This method decomposes a vector field into three components: curl-free, divergence-free and harmonic. The curl-free and divergence-free components are obtained through scalar potentials given by discrete Poisson equations.

Our method uses the *Smoothed Particle Hydrodynamics* (SPH) framework to obtain a smooth approximation of the differential operators utilized in Poisson equation. The SPH Poisson equation applied to each particle of the domain

discretization results in a highly sparse linear system. Its solution is a scalar potential that defines a component of the decomposition.

The Helmholtz-Hodge decomposition is traditionally an important tool of visualization and analysis of vector fields, which is here extended to meshless representations. Moreover, this method provides a new numerical tool to enforce incompressibility in SPH fluid flow simulations.

The authors intend to extend this work to decompose tri-dimensional vector fields where the divergence-free component is given by a vector potential. The linear system obtained in 3D case is larger and sparser than the 2D case, requiring further efforts to ensure the numerical stability of the system.

Acknowledgments

(a) $t = 0$ sec.   (b) $t = 2$ sec.   (c) $t = 4$ sec.   (d) $t = 6$ sec.
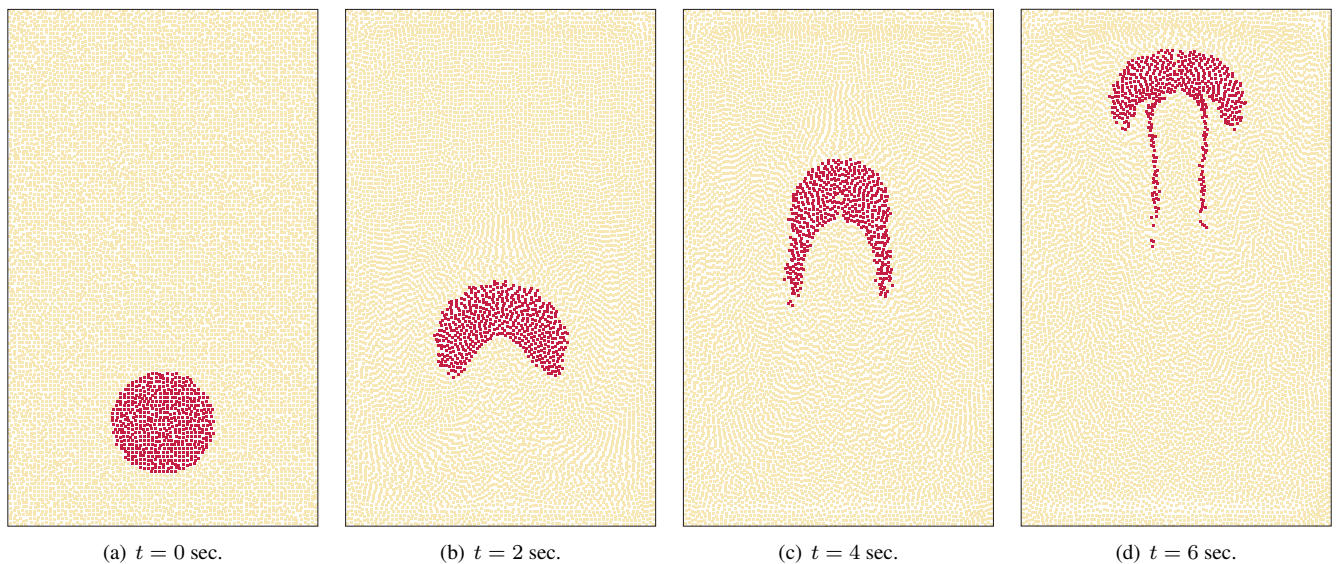
Figure 18: *Rising of a light fluid droplet (dark red) in a heavy fluid (orange) using* **SPH-HH** *method with* 10500 *particles. The heavy fluid is twice denser than the light fluid.*

References

[1] M. Becker and M. Teschner. Weakly compressible SPH for free surface flows. In *Symposium on Computer Animation*, pages 209–217, 2007.

[2] R. Bridson, J. Houriham and M. Nordenstam. Curl-noise for procedural fluid flow. *ACM Transactions on Graphics*, 26(3), 2007.

[3] G. Chen, K. Mischaikow, R. S. Laramee and E. Zhang. Efficient morse decompositions of vector fields. *IEEE Transactions on Visualization and Computer Graphics*, 14(4):848–862, 2008.

[4] A. Chorin and J. Marsden. *A Mathematical Introduction to Fluid Mechanics*. Springer, 1992.

[5] F. Colin, R. Egli and F. Y. Lin. Computing a null divergence velocity field using smoothed particle hydrodynamics. *Journal of Computational Physics*, 217(2):680–692, 2006.

[6] A. Cuzol, P. Hellier and E. Mémin. A low dimensional fluid motion estimator. *International Journal on Computer Vision*, 75(3):329–349, 2007.

[7] J. Dongarra, A. Lumsdaine, R. Pozo and K. Remington. IML++ v. 1.2 - iterative methods library, user's guide, 1996. http://math.nist.gov/iml++/.

[8] D. Dunbar and G. Humphreys. A spatial data structure for fast poisson-disk sample generation. In *Siggraph*, pages 503–508, 2006.

[9] C. Diaz-Goano, P. D. Minev and K. Nandakumar. A fictitious domain/finite element method for particulate flows. *Journal of Computational Physics*, 192(1):105 – 123, 2003.

[10] Q. Guo., M. K. Mandal and M. Y. Li. Efficient Hodge-Helmholtz decomposition of motion fields. *Pattern Recognition Letters*, 26(4):493–501, 2005.

[11] J. Helman and L. Hesselink. Representation and display of vector field topology in fluid flow data sets. *Computer*, 22(8):27–36, 1989.

[12] A. Hoerl and R. Kennard. Ridge regression: Biased estimation for nonorthogonal problems. *Technometrics*, 12(1):55–67, 1970.

[13] M. Lage, F. Petronetto, A. Paiva, H. Lopes, T. Lewiner and G. Tavares. Vector field reconstruction from sparse samples with applications. In *Sibgrapi*, pages 297–304. IEEE, 2006.

[14] F. Petronetto. Equação de Poisson e a Decomposição de Helmholtz-Hodge usando sph. PhD thesis, *PUC–Rio*, 2008.

[15] K. Polthier and E. Preuss. Variational Approach to Vector Field Decomposition. In *Eurographics Workshop on Scientific Visualization*. Springer, 2000.

[16] K. Polthier and E. Preuss. Identifying vector fields singularities using a discrete Hodge decomposition. In *Visualization and Mathematics III*, pages 113–134. Springer, 2003.

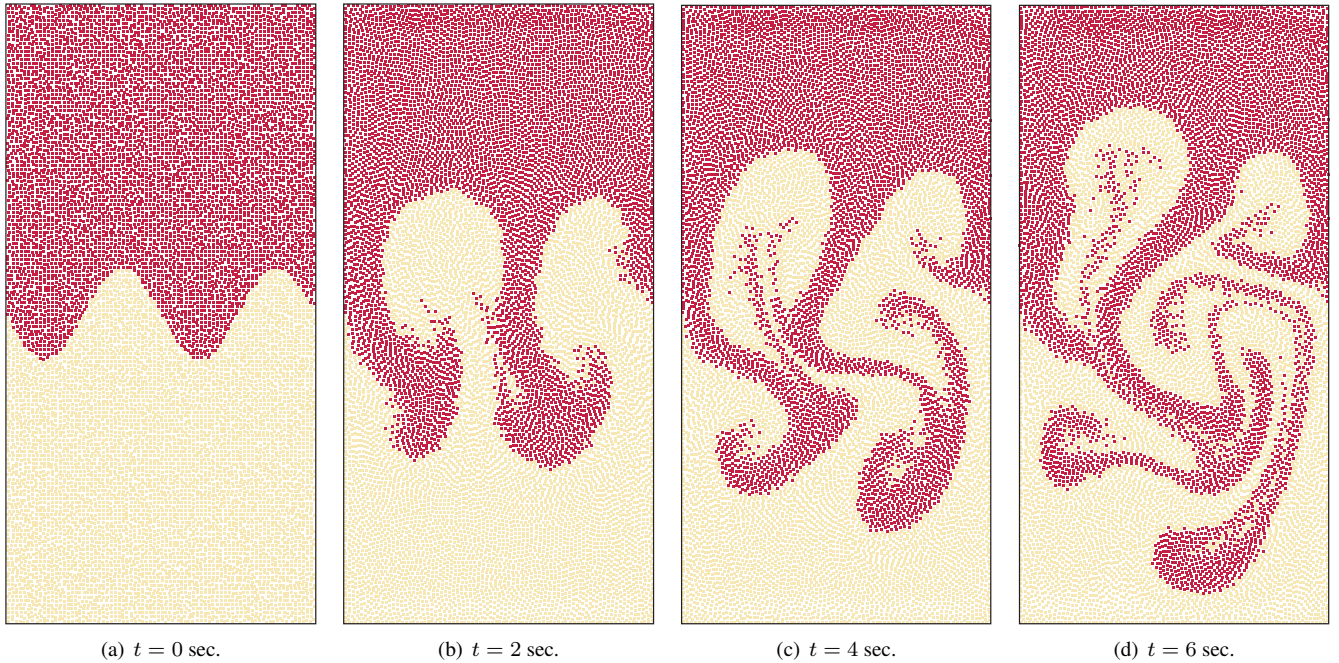[17] R. Pozo and K. Remington. SparseLib++ v. 1. 5 - sparse matrix class library, user's guide, 1996. http://math.nist.gov/sparselib++/.

(a) $t = 0$ sec.   (b) $t = 2$ sec.   (c) $t = 4$ sec.   (d) $t = 6$ sec.

Figure 19: *Simulation of Rayleigh-Taylor instabilities of a heavy fluid (dark red) above light (orange) using* **SPH-HH** *method with* 12500 *particles. The heavy fluid is 1.2 times denser than the light fluid.*

[18] Y. Saad. *Iterative Methods for Sparse Linear Systems*. SIAM, 2003.

[19] J. Stam. Stable fluids. In *Siggraph*, pages 121–128, 1999.

[20] Y. Tong, S. Lombeyda, A. N. Hirani and M. Desbrun. Discrete multiscale vector field decomposition. *ACM Transactions on Graphics*, 22(3):445–452, 2003.

[21] X. Tricoche, G. Scheuermann and H. Hagen. Continuous topology simplification of planar vector fields. In *Visualization*, pages 159–166. IEEE, 2001.

[22] S. J. Cummins and M. Rudman. An SPH projection method. *Journal of Computational Physics*, 152(2):584–607, 1999.

[23] R. Keiser, B. Adams, D. Gasser, P. Bazzi, P. Dutré and M. Gross. A unified lagrangian approach to solid-fluid animation. In *Symposium on Point-Based Graphics*, pages 125–134, 2005.

[24] S. Li and W. K. Liu. *Meshfree Particle Methods*. Springer, 2004.

[25] G. R. Liu and M. B. Liu. *Smoothed Particle Hydrodynamics*. World Science, 2005.

[26] J. J. Monaghan. Smoothed particle hydrodynamics. *Reports on Progress in Physics*, 68:1703–1759, 2005.

[27] M. Müller, D. Charypar and M. Gross. Particle-based fluid simulation for interactive applications. In *Symposium on Computer Animation*, pages 154–159, 2003.

[28] M. Müller, B. Solenthaler, R. Keiser and M. Gross. Particle-based fluid-fluid interaction. In *Symposium on Computer Animation*, pages 237–244, 2005.

[29] A. Paiva, F. Petronetto, T. Lewiner and G. Tavares. Particle-based non-Newtonian fluid animation for melting objects. In *Sibgrapi*, pages 78–85, 2006.